Acta Crystallographica Section B
Structural Science
ISSN 0108-7681

Crystal chemistry of mimetite, $Pb_{10}(AsO_4)_6Cl_{1.48}O_{0.26}$, and finnemanite, $Pb_{10}(AsO_3)_6Cl_2$

Tom Baikie,[a]* Cristiano Ferraris,[a,b] Wim T. Klooster,[a,c] S. Madhavi,[a] Stevin S. Pramana,[a] Allan Pring,[d] G. Schmidt[d] and T. J. White[a]

[a] School of Materials Science and Engineering, Nanyang Technological University, Block N4.1, 50 Nanyang Avenue, Singapore 639798, [b]Laboratoire de Minéralogie, USM 201, Muséum National d'Histoire Naturelle, CP 52, 61 Rue Buffon, 75005 Paris, France, [c]Institute of Materials Research and Engineering, 3 Research Link, Singapore 117602, and [d]Department of Mineralogy, South Australian Museum, North Terrace, Adelaide, Australia

Correspondence e-mail: tbaikie@ntu.edu.sg

Received 22 October 2007
Accepted 11 December 2007

The crystal chemistries of synthetic mimetite, $Pb_{10}(As^{5+}O_4)_6(Cl_{2-x}O_{x/2})$, a neutral apatite, and finnemanite, $Pb_{10}(As^{3+}O_3)_6Cl_2$, a reduced apatite, were characterized using a combination of X-ray powder diffraction, neutron diffraction, transmission electron microscopy and X-ray photoelectron spectroscopy. Both phases conform to hexagonal $P6_3/m$ symmetry; however, the temperature-driven transformation of clinomimetite to mimetite described earlier was not confirmed. The average mimetite structure is best described through the introduction of partially occupied oxygen sites. A better understanding of the mixed arsenic speciation in apatites can guide the formulation of waste form ceramics and improve models of long-term durability after landfill disposal.

1. Introduction

Anthropogenic releases of lead and arsenic oxides from mineral resources present a health risk to surrounding populations and the environment. A sustainable approach for treating these pollutants is to close their metal cycles through crystallochemical fixation in the lithosphere (White & Toor, 1996). Members of the apatite family are emerging as important immobilization matrices because they can incorporate a range of toxic elements, and with appropriate placement, will be physically and chemically durable over eons. The familiar neutral apatite genus $A(1)_4A(2)_6(BO_4)_6X_2$ (A = large cations; B = metalloids; X = anions and oxyanions) usually conforms to $P6_3/m$ symmetry (Pramana *et al.*, 2008), and more than 70 discrete species are recognized (White *et al.*, 2005). This compositional diversity can be accommodated in three ways. First, an adaptable $A(1)_4(BO_4)_6$ microporous framework circumscribes one-dimensional tunnels that expand or contract according to the filling characteristics of the $A(2)_6X_2$ component (White & Dong, 2003). Second, the BO_4 tetrahedra are essentially rigid bodies, and should the tunnel be sub-stoichiometric or contain smaller ions, these units rotate to satisfy bond-valence requirements while preserving the framework topology (Baikie *et al.*, 2007). Finally, oxidized and reduced genera exist in which the BO_4 tetrahedra are replaced by BO_3 and BO_5 polyhedra, and hybrids such as $La_{10}(GeO_4)_5(GeO_5)O_2$ are known (Pramana *et al.*, 2007).

The commonly encountered waste-management apatite species are mimetite, $Pb_{10}(AsO_4)_6Cl_2$, turneaurite, $Ca_{10}[(As,P)O_4]_6Cl_2$, phosphohedyphane, $Ca_4Pb_6(PO_4)_6Cl_2$ (Kampf *et al.*, 2006), and pyromorphite, $Pb_{10}(PO_4)_6Cl_2$, with Cl^- partially replaced by OH^- and F^-. Synthetic analogues show a complete solid solution of As^{5+} and P^{5+}. Mimetite is dimorphic, and aside from the usual $P6_3/m$ symmetry, also

Table 1
Refined atomic coordinates for mimetite $Pb_{10}(AsO_4)_6Cl_{1.48}O_{0.26}$.

Space group $P6_3/m$; a = 10.2055 (2), c = 7.4483 (2) Å; R_{wp} = 0.058 and R_B = 0.019.

Site	Wyckoff	x	y	z	B	Occ.
Pb1	4(*f*)	1/3	2/3	0.0073 (4)	1.3 (1)	1.0
Pb2	6(*h*)	0.2491 (2)	0.0027 (3)	1/4	1.4 (1)	1.0
As1	6(*h*)	0.4060 (3)	0.3822 (3)	1/4	1.2 (1)	1.0
O1	6(*h*)	0.3268 (4)	0.4932 (4)	1/4	1.7 (1)	1.0
O2†	12(*i*)	0.5965 (4)	0.4851 (5)	0.2193 (10)	1.9 (1)	0.5
O3*a*	12(*i*)	0.3306 (6)	0.2444 (6)	0.0917 (6)	1.2 (1)	0.5
O3*b*	12(*i*)	0.3847 (6)	0.2953 (6)	0.0501 (10)	1.6 (1)	0.5
Cl	2(*b*)	0	0	0	1.5 (1)	0.74
O4	2(*a*)	0	0	1/4	2.5 (2)	0.13

† In $P6_3/m$ this position is also generated at (0.5965, 0.4851, 0.2807).

adopts the less well characterized low-temperature $P112_1/b$ clinomimetite form that may arise owing to displacement of the locus of the stereochemically active $Pb(1)^{2+}$ $6s^2$ lone-pair electrons (Dai *et al.*, 1991). This structural adaptation is distinct from the monoclinic ($P112_1/b$) dimorphs of chlorapatite, $Ca_{10}(PO_4)_6Cl_2$ (Mackie *et al.*, 1972; Bauer & Klee, 1993), and hydroxyapatite, $Ca_{10}(PO_4)_6(OH)_2$ (Elliott *et al.*, 1973; Suetsugu & Tanaka, 2002), that evolve from ordered *X*-anion displacements. Keppler (1968, 1969) also found that both natural and synthetic samples of mimetite undergo a spontaneous and reversible monoclinic to hexagonal transition over the temperature range 371–393 K. However, a single-crystal neutron diffraction study on a natural sample of mimetite failed to reveal any evidence of the monoclinic form (Calos & Kennard, 1990). The different structural reports found in the literature and the range of transition temperatures found by Keppler suggests that the monoclinic/hexagonal phase transition of mimetite is compositionally dependent. Finnemanite, $Pb_{10}(As^{3+}O_3)_6Cl_2$, can be regarded as an oxygen-deficient mimetite, where arsenic is completely reduced to the trivalent state (Effenberger & Pertlik, 1979; see Fig. 1). This article describes the synthesis, chemistry and crystal structures of $Pb_{10}(As^{5+}O_4)_6Cl_{1.48}O_{0.26}$ and $Pb_{10}(As^{3+}O_3)_6Cl_2$, including the dilation of mimetite with heating.

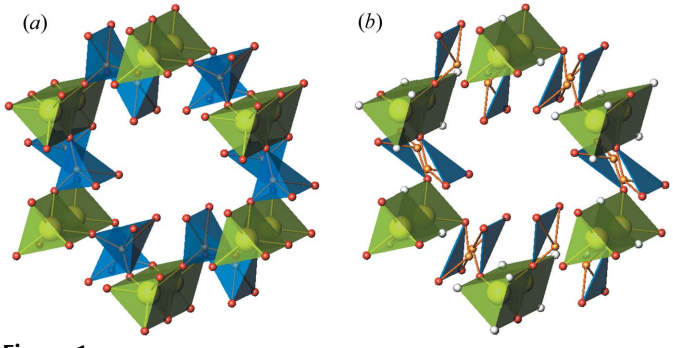

Figure 1
Idealized structural representations of (*a*) mimetite and (*b*) finnemanite. Indicated are the $Pb(1)O_6$ polyhedra (green) and the tetrahedral and triangular coordination of As^{5+} and As^{3+} (blue), respectively. Indicated in white are the O atoms which are present in mimetite but absent in finnemanite.

2. Experimental methods

2.1. Synthesis of mimetite

Stoichiometric proportions of high-purity PbO, As_2O_3 and $PbCl_2$ were manually ground in an agate mortar and pestle for 30 min, pressed into pellets and placed in alumina crucibles with a loose-fitting alumina lid. A small quantity of $PbCl_2$ spread around the base of the alumina crucible, but not in contact with the reagents, created a chlorine-rich atmosphere to minimize volatilization. The materials were heated at 973 K for 12 h, re-ground and re-pressed into pellets, then treated for a further 12 h at the same temperature.

2.2. Synthesis of finnemanite

2.2.1. High-temperature route. High-purity PbO, As_2O_3 and $PbCl_2$ were mixed stoichiometrically in a Schlenk tube in argon, dried under vacuum at 323 K for 1 h, and then heated at 973 K for 10 min. The product was a brown viscous melt that crystallized as grey finnemanite upon quenching to room temperature. Finnemanite was oxidized to mimetite by heating in air to 723 K. However, the reaction was irreversible and attempts to prepare finnemanite by the reduction of mimetite in a stream of N_2/H_2 (95%:5%) at various temperatures were unsuccessful and invariably yielded an amorphous product.

2.2.2. Low-temperature route. Stoichiometric proportions of PbO, As_2O_3 and HCl were stirred in water at 323 K for 24 h, during which the colour of the suspension changed from yellow to grey. The slurry was filtered, washed with either methanol, distilled water or acetone then dried for 2 h at a temperature in the range 343–393 K. Low-temperature synthesis of finnemanite proved more reliable than the high-temperature method, however, control of the washing and drying conditions were critical. If washed in water and dried at 393 K for 2 h the finnemanite underwent partial oxidation with $\sim$25% of the As^{3+} transforming to As^{5+}. Washing in acetone and drying at 333 K for 2 h resulted in a reduced product (as indicated by the chemical speciation derived from X-ray photoelectron spectroscopy) whose X-ray diffraction poorly matched finnemanite. For reasons that are presently unclear, subsequent air oxidation at 973 K led to a smaller weight increase than expected, perhaps associated with the particle size or amorphous by-products. The purest finnemanite resulted from washing the slurry in methanol and drying at 343 K for 2 h.

2.3. Crystallographic characterization

Neutron powder diffraction data of finnemanite and mimetite were collected on the high-resolution powder diffractometer (HRPD) at the high-flux Australian reactor

Table 2
Selected bond lengths (Å) and angles (°) for mimetite $Pb_{10}(AsO_4)_6Cl_{1.48}O_{0.26}$ at room temperature.

Pb1—O1	2.508 (3)
Pb1—O2	2.622 (6), 2.937 (6)
Pb1—O3*b*	2.739 (6)
Pb1—O3*a*	3.165 (6)
Pb2—O2	2.373 (4)
Pb2—O3*a*	2.473 (6), 2.694 (5)
Pb2—O3*b*	2.561 (5), 2.985 (6)
Pb2—O4	2.528 (4)
Pb2—Cl	3.140 (6)
As—O1	1.689 (6)
As—O2	1.700 (4)
As—O3*a*	1.694 (5)
As—O3*b*	1.688 (5)
O2—O2	0.457 (14)
O3*a*—O3*b*	0.619 (4)
O1—As—O2	111.6 (2)
O1—As—O3*a*	112.6 (3)
O1—As—O3*b*	111.9 (2)
O2—As—O3*a*	108.9 (2), 120.7 (2)
O2—As—O3*b*	90.8 (2), 104.5 (2)
O3*a*—As—O3*b*	21.1 (2)
O2—As—O2	15.5 (5)

(HIFAR) operated by the Australian Nuclear Science and Technology Organization (ANSTO). A neutron wavelength of 1.883 (1) Å was used from 0.029 to 150.079° 2θ in 0.05° steps. Approximately 15 g of each apatite was loaded into a 12 mm diameter vanadium can (stainless steel for the high-temperature data) that was rotated during data collection. Rietveld refinements were performed with *TOPAS* (Bruker AXS, 2005) using a pseudo-Voigt peak-shape corrected for asymmetry. The scattering lengths of Pb, As, O and Cl were 0.9405, 0.6580, 0.5803 and 0.9577 $\times$ 10^{-12} cm, respectively (Sears, 1993). The reported hexagonal to monoclinic phase transition of mimetite at $\sim$ 373 K (Dai *et al.*, 1991) was investigated by collecting neutron diffraction data *in situ* at 298, 373, 423 and 473 K.

Powder X-ray diffraction patterns were collected using a Shimadzu diffractometer (Cu $K\alpha$ radiation) over the angular range 10–140° 2θ with a step size of 0.02° and a dwell time of 10 s per step. The patterns were analysed by the Rietveld method using the fundamental parameters approach (Cheary & Coelho, 1992) contained within *TOPAS* (Bruker AXS, 2005).[1]

Powdered samples deposited on holey carbon copper grids were analysed using transmission electron microscopy (TEM) with a JEOL JEM 2100F instrument equipped with a double-tilt holder. Field-limiting apertures for selected-area electron diffraction (SAED) were 5, 20 and 60 µm in diameter. High-resolution images were collected using a high-contrast objective aperture of 20 µm, corresponding to a nominal point-to-point resolution of 0.17 nm. Electron-diffraction patterns were calibrated repeatedly using external standards to derive reliable values for both the electron wavelength and camera length, so that the cell parameters are accurate to better than $\pm$ 1%, while for angles, the errors are $\pm$ 0.2%.

The simulation of high-resolution transmission electron microscope (HRTEM) images was performed using *JEMS* (Stadelmann, 2003). For all the models tested, the calculations employed identical specimen characteristics (thickness and orientation), illumination conditions and objective lens defocus values, verified by comparison with the contrast transfer function. The simulation conditions were reproduced exactly for each crystal structure model.

2.4. X-ray photoelectron spectroscopy (XPS)

The chemical states of arsenic in $Pb_{10}(AsO_3)_6Cl_2$ and $Pb_{10}(AsO_4)_6Cl_{1.48}O_{0.28}$ were examined by X-ray photoelectron spectroscopy (XPS) using a PHI 5600 spectrometer. Samples were dusted onto a polymeric-based adhesive tape and spectra recorded using Mg $K\alpha_1$ excitation over the binding-energy range 0–1000 eV. High-resolution spectra for As (3*d*), Pb (4*f*), Cl (2*p*) and C (1*s*) were collected in their respective energy ranges (Wagner *et al.*, 1978). The XPS analysis chamber was maintained at a pressure of 8.0 $\times$ 10^{-9} torr. Peak deconvolution and fitting of the spectra were carried out with *Casa*, Version 2.3.10 (computer-aided surface analysis; Fairley & Carrick, 2005). Binding-energy values were referenced against

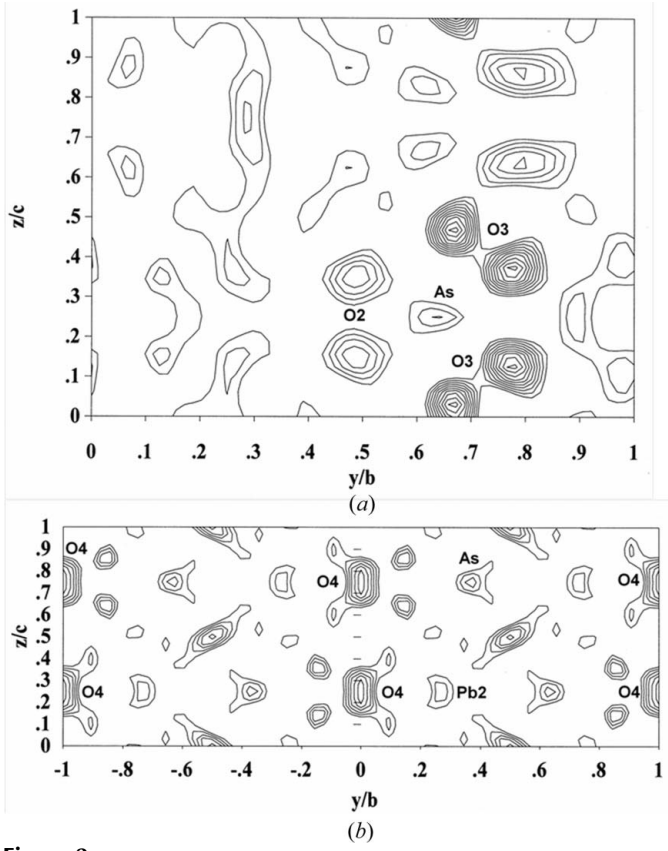

Figure 2
[100] difference-Fourier maps at (*a*) x = 0.0781 and (*b*) at x = 0 from a refinement of mimetite in the space group $P6_3/m$. (*a*) Area of excess nuclear density indicating the splitting of the O2 and O3 atoms; (*b*) areas of excess nuclear density indicated near (0, 0, $\frac{1}{4}$) of the apatite channel, which is a site commonly occupied by smaller anions such as oxygen.

[1] Supplementary data for this paper are available from the IUCr electronic archives (Reference: LM5013). Services for accessing these data are described at the back of the journal.

adventitious carbon (C 1*s* = 284.8 eV). Curve fitting of the As (3*d*) lines employed a Voigt function with 30% Lorentzian character and a Shirley background.

3. Structure of mimetite $Pb_{10}(AsO_4)_6(Cl_{2-x}O_{x/2})$

3.1. Room-temperature powder neutron and X-ray diffraction

Initial refinements of room-temperature powder neutron diffraction data for mimetite $Pb_{10}(AsO_4)_6Cl_2$ used the space group $P6_3/m$. Although, this model gave a satisfactory fit (R_{wp} = 0.094 and R_B = 0.064), the reliability factors and difference plot were superior when a model based on the monoclinic space group $P112_1/b$ clinomimetite was used (R_{wp} = 0.064, R_B = 0.028). However, unrealistic As—O bond lengths and large thermal parameters disqualified this structural model. Refinements were attempted whereby a soft constraint was imposed on the As—O bond lengths; however, this gave an inferior fit and resulted in unrealistic tetrahedron bond angles. To discover the cause, a difference-Fourier map from the $P6_3/m$ model was generated and revealed a clear discrepancy in nuclear density around the O3-atom positions, together with splitting of the O2 site (Fig. 2). In addition, excess nuclear density between the Cl atoms along the *c* axis where smaller anions generally reside suggests limited insertion of O^{2-} at 2(*a*) ($00\frac{1}{4}$). Partial $2Cl^- \leftrightarrow O^{2-}$ substitution is also consistent with ~ 75% occupancy of Cl at 2(*b*) (0,0,0) in the $P6_3/m$ model and is expected for the maintenance of overall charge neutrality due to the loss of Cl.

The $P6_3/m$ mimetite model was modified to address these deficiencies. First, a significant improvement in fitting (R_{wp} = 0.069 R_B = 0.026) was achieved by splitting the O3 into two sites each with 50% occupancy. Second, the O2 atom was released to the 12(*i*) general position with 50% tenancy, which again improved the reliability factors (R_{wp} = 0.067, R_B = 0.023). Finally, a partial oxygen was introduced at (0, 0, $\frac{1}{4}$) of the apatite channel, with the overall occupancy of chlorine and oxygen content constrained to maintain charge neutrality. This yielded a superior result (R_{wp} = 0.058 R_B = 0.019) and the final crystallographic parameters are collated in Table 1. It is possible that rather than oxygen located at (0, 0, $\frac{1}{4}$) the Fourier map could indicate that hydroxyl groups are located at this site. Neutrons are particularly sensitive at locating protons, which have a negative scattering factor; however, any attempt to introduce a proton near this site resulted in inferior fits, indicating that they were not present. It is apparent that the refined displacement parameters of Pb and As are quite large, consistent with static disorder arising from degeneracy of the oxygen sites. Selected bond lengths and angles are summarized in Table 2 and the refined neutron profile shown in Fig. 3(*a*).

Due to the inherently larger peak widths associated with neutron diffraction, the mimetite was also examined by powder X-ray diffraction, which offers a

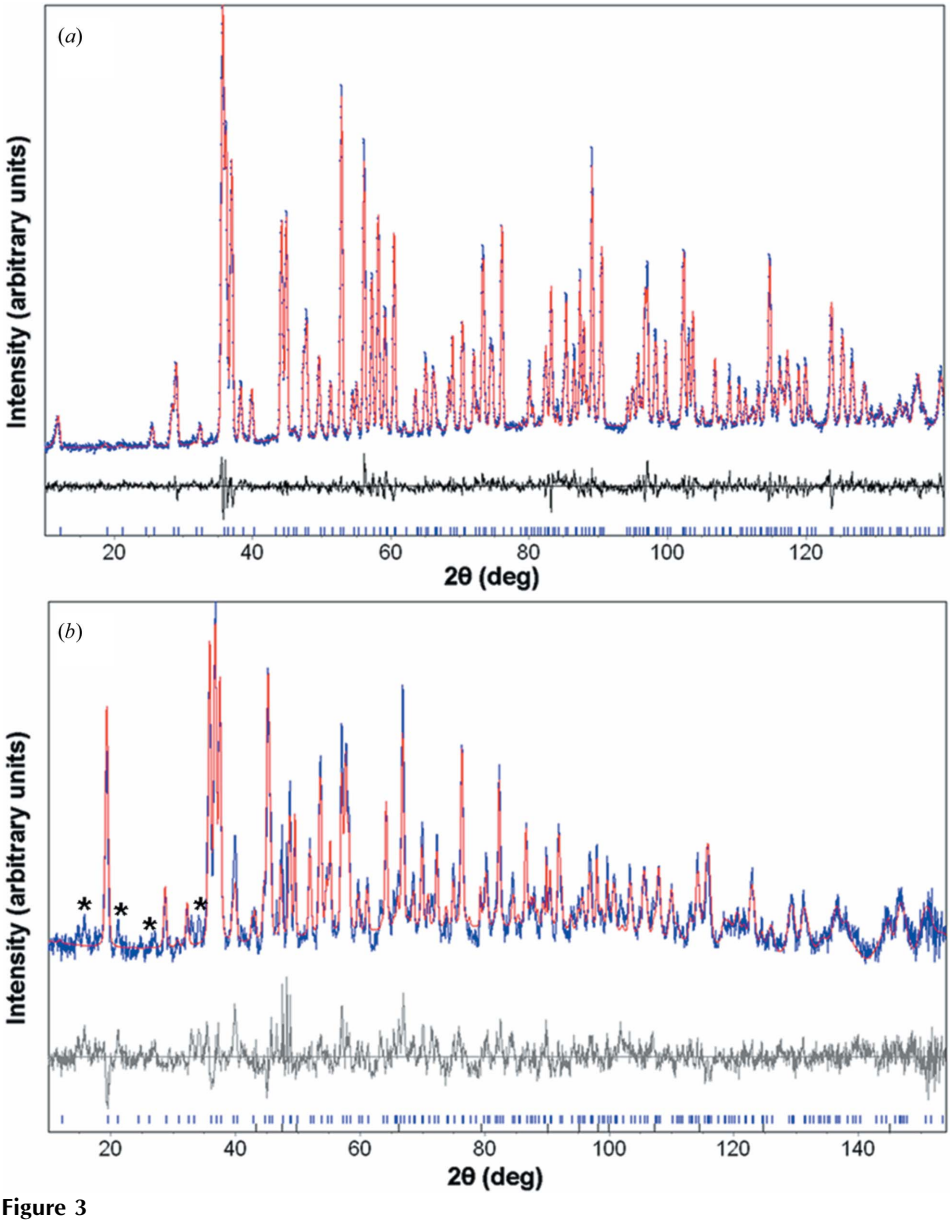

Figure 3
Room-temperature Rietveld refinement profiles of the powder neutron diffraction data for (*a*) mimetite and (*b*) finnemanite. * indicates reflections associated with the secondary phase in finnemanite.

Table 3
Experimental details.

	$As_6Cl_2O_{18}Pb_{10}$	$As_6Cl_{1.48}O_{24.26}Pb_{10}$ 298 K	$As_6Cl_{1.48}O_{24.26}Pb_{10}$ 373 K	$As_6Cl_{1.48}O_{24.26}Pb_{10}$ 423 K	$As_6Cl_{1.48}O_{24.26}Pb_{10}$ 473 K
Crystal data					
Chemical formula	$As_6Cl_2O_{18}Pb_{10}$	$As_6Cl_{1.48}O_{24.26}Pb_{10}$	$As_6Cl_{1.48}O_{24.26}Pb_{10}$	$As_6Cl_{1.48}O_{24.26}Pb_{10}$	$As_6Cl_{1.48}O_{24.26}Pb_{10}$
M_r	2880.43	2962.16	2962.16	2962.16	2962.16
Cell setting, space group	Hexagonal, $P6_3/m$	Hexagonal, $P6_3/m$	Hexagonal, $P6_3/m$	Hexagonal, $P6_3/m$	Hexagonal, $P6_3/m$
Temperature (K)	298	298	373	423	473
a, c (Å)	10.2972 (6), 7.0690 (6)	10.2055 (2), 7.4483 (2)	10.2224 (3), 7.4494 (2)	10.2323 (3), 7.4533 (2)	10.2415 (3), 7.4594 (2)
V (Å^3)	649.12 (8)	671.83 (3)	674.15 (3)	675.82 (3)	677.59 (3)
Z	1	1	1	1	1
D_x (Mg m^{-3})	7.369	7.322	7.296	7.278	7.259
Radiation type	Neutron	Neutron	Neutron	Neutron	Neutron
Specimen form, colour	Cylinder, grey	Cylinder, white	Cylinder, white	Cylinder, white	Cylinder, white
Specimen preparation cooling rate (K min^{-1})	–	100	100	100	100
Specimen preparation pressure (kPa)	100	100	100	100	100
Specimen preparation temperature (K)	323	973	973	973	973
Data collection					
Diffractometer	Local	Local	Local	Local	Local
Data collection method	Specimen mounting: vanadium can with He exchange gas; mode: reflection; scan method: fixed	Specimen mounting: vanadium can with He exchange gas; mode: reflection; scan method: fixed	Specimen mounting: vanadium can with He exchange gas; mode: reflection; scan method: fixed	Specimen mounting: vanadium can with He exchange gas; mode: reflection; scan method: fixed	Specimen mounting: vanadium can with He exchange gas; mode: reflection; scan method: fixed
2θ (°)	$2\theta_{min}$ = 10, $2\theta_{max}$ = 150, increment = 0.05	$2\theta_{min}$ = 10, $2\theta_{max}$ = 150, increment = 0.05	$2\theta_{min}$ = 10, $2\theta_{max}$ = 150, increment = 0.05	$2\theta_{min}$ = 10, $2\theta_{max}$ = 150, increment = 0.05	$2\theta_{min}$ = 10, $2\theta_{max}$ = 150, increment = 0.05
Refinement					
R factors and goodness-of-fit	R_p = 0.060, R_{wp} = 0.077, R_{exp} = 0.090, R_B = 0.034, S = 0.86	R_p = 0.046, R_{wp} = 0.058, R_{exp} = 0.090, R_B = 0.019, S = 0.65	R_p = 0.043, R_{wp} = 0.055, R_{exp} = 0.088, R_B = 0.017, S = 0.63	R_p = 0.045, R_{wp} = 0.057, R_{exp} = 0.089, R_B = 0.019, S = 0.65	R_p = 0.049, R_{wp} = 0.062, R_{exp} = 0.011, R_B = 0.019, S = 0.58
Wavelength of incident radiation (Å)	1.8834	1.8834	1.8834	1.8834	1.8834
Excluded region(s)	0.027–10° unreliable due to background	0.027–10° unreliable due to background	0.027–10° unreliable due to background	0.027–10° unreliable due to background	0.027–10° unreliable due to background
Profile function	Pseudo-Voigt	Pseudo-Voigt	Pseudo-Voigt	Pseudo-Voigt	Pseudo-Voigt
No. of parameters	20	45	48	48	48
Weighting scheme	Based on measured s.u.s	Based on measured s.u.s	Based on measured s.u.s	Based on measured s.u.s	Based on measured s.u.s
$(\Delta/\sigma)_{max}$	< 0.0001	< 0.0001	< 0.0001	< 0.0001	< 0.0001

Computer programs used: local, Shimadzu XRD 6000, *TOPAS* (Bruker AXS, 2005), *ATOMS* (Dowty, 2002), *GFOURIER* (Gonzales-Platas & Rodriguez-Carvajal, 2006).

higher peak resolution. The structural model derived from the neutron diffraction yielded an excellent fit to the X-ray data with no evidence of a departure from the hexagonal metric.

3.2. Temperature dependence

At 373, 423 and 473 K the lattice parameters dilate successively (see Table 3 and Fig. 4), while the distances between the split oxygen sites decrease (see Table 4), with the expectation that these will merge at higher temperatures providing mimetite remains stable. No convincing evidence of a monoclinic to hexagonal phase transformation was obtained; however, this transition should not be discounted at temperatures below ambient.

The metaprism twist (φ) angle, defined as the (001) projected angle of O1—A—O2, is a useful tool to verify that refined apatite structures are crystallographically realistic, with the degree of rotation related to the relative sizes of the A, B and X ions (White *et al.*, 2005; Fig. 1). The twist angle φ decreases with increasing temperature as the tunnel diameter expands to accommodate the relatively larger X anions (Cl^- and O^{2-}), that in turn results in a greater expansion of the a parameter compared with the c parameter. The increase in the a parameter is linear (Fig. 4), however, the change in c is more complex possibly due to distortion caused by the $Pb(1)^{2+}$ lone pair.

3.3. Electron diffraction and imaging

While the neutron diffraction model provides the average structure, it is possible that regions compliant with $P6_3/m$ will exist on the unit-cell scale without recourse to statistical filling of oxygen sites. Precedents for such nanodomains include the $(Pb_{10-x}Ca_x)(VO_4)_6F_2$ synthetic vanadinites (Dong *et al.*,

Table 4
O2—O2 and O3*a*—O3*b* splitting distances as a function of temperature.

Temperature (K)	O2—O2	O3*a*—O3*b*
Room temperature (~ 298 K)	0.46 (1)	0.619 (4)
373	0.41 (2)	0.569 (4)
423	0.43 (2)	0.535 (8)
473	0.42 (2)	0.538 (7)

Table 5
Refined atomic coordinates for finnemanite.

Space group: $P6_3/m$; a = 10.2972 (6), c = 7.0690 (6) Å; R_{wp} = 0.077, R_B = 0.034.

Site	*x*	*y*	*z*	*B*	Occ.
Pb1	1/3	2/3	0.9937 (12)	1.0 (1)	1
Pb2	0.2644 (6)	0.0360 (7)	1/4	1.0 (1)	1
As	0.4095 (11)	0.4033 (12)	1/4	1.2 (1)	1
O1	0.6076 (12)	0.4653 (12)	1/4	1.0 (1)	1
O2	0.3703 (8)	0.2789 (8)	0.0568 (9)	1.0 (1)	1
Cl	0	0	0	1.7 (3)	1

Table 6
Selected bond distances (Å) and angles (°) for finnemanite.

Pb1—O1	2.452 (11)
Pb1—O2	2.836 (8)
Pb2—O1	2.429 (12)
Pb2—O2	2.566 (9)
As—O1	1.808 (16)
As—O2	1.775 (10)
Pb2—Cl	3.109 (9)
O1—As—O2	93.7 (6)
O2—As—O2	100.6 (8)

Table 7
Bond-valence sums for mimetite and finnemanite.

	Mimetite	Finnemanite
Pb1	1.72	1.61
Pb2	1.87	1.96
As	4.88	3.03

2005) and fluorapatite gems (Ferraris *et al.*, 2005). In the case of mimetite, SAED patterns were collected from $[001]_{hex}$ and $[100]/[010]_{hex}$ zones, and additionally higher-index axes were examined to verify the extinction conditions and possible distortion of the hexagonal metric (Fig. 5). Whereas $[001]_{hex}$ did not show any exceptions to $P6_3/m$ systematic absences, the [100]/[010] patterns contain $b^*/2$ periodicity and a plausible doubling of the cell edge (~ 20.2 Å *versus* 10.1 Å; Figs. 5*c* and *e*). However, as these supercell reflections were absent in [001] zones their origin must be dynamical, even if the monoclinic cell $P112_1/b$ of Dai *et al.* (1991) is assumed. It is believed that multiple scattering is weak when the crystals are viewed along [001] as in this projection, parallel to the tunnel, the electron potential is less dense. However, perpendicular to [001] stronger scattering will occur as electrons traverse $Pb(1)O_6$ metaprisms and $Pb(2)O_6Cl_2$ polyhedra.

Although dynamical doubling is consistent with the ordering of oxygen over the split O3 position, it is not possible to exclude a statistical distribution as implied from the neutron study. Neither experimental nor simulated HRTEM [100] zone-axis images show a real-space doubling of *b*, notwithstanding the stronger dynamical effects (Figs. 5*d* and *f*). Simulation of two models – one containing split 12(*i*) O3 and the other a single 6(*h*) position – inevitably failed to duplicate *b* doubling (Figs. S1*b*, *c*, *f* and *g* of the supplementary material). This is attributed to the greater phase contrast arising from heavy atomic species (*i.e.* As and Pb), that obscures a supercell contribution from oxygen.

Comparing the [001] experimental and calculated HRTEM images there are evident differences in contrast distribution related to the projected spatial arrangements of $[AsO_4]^{3-}$ and $[Pb(1)O_6]^{10-}$ groups (see Fig. S1*a* of the supplementary material), however, it was not possible to develop a superior model through image simulation. Looking to the HRTEM image of Fig. S1(*a*) there are evidently brighter areas aligned parallel to [010]. Attempts to reproduce the same brightness distribution by varying both specimen (*e.g.* thickness) and microscope (*e.g.* beam tilting) conditions were tested without success. In the same image, differences between the projected atomic columns of $[AsO_4]^{3-}$ and $[Pb(1)O_6]^{10-}$ are evident, and it is tentatively suggested that these observations argue in favour of the O3 split model (white circles in Figs. S1*a* and *b*). While the image simulation of $P6_3/m$ and $P112_1/b$ models along [001] shows that differentiation is not feasible, the doubled *b* axis for a monoclinic cell is striking in [100] (Figs. S1*d* and *h*). As the [100] experimental images never contain characteristic clinomimetite contrast this dimorph can be excluded.

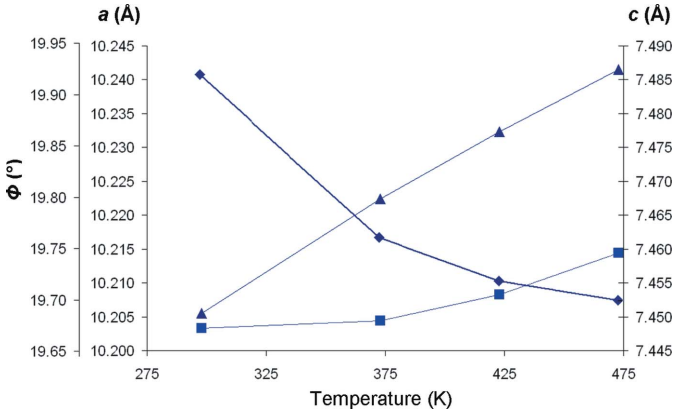

Figure 4
Plot of the lattice parameters and metaprism twist angles for mimetite at room temperature, 373, 423 and 473 K. The twist angles are represented by diamonds, and the triangles and squares are the *a* and *c* parameters, respectively.

4. Structure of finnemanite, $Pb_{10}(AsO_3)_6Cl_2$

The refined structure for finnemanite synthesized using the methanol washing method gave a good fit to $P6_3/m$ (Fig. 3*b*). A small number of reflections evident in the powder pattern could not be assigned to the finnemanite structure, nor were

they consistent with a supercell arising from a doubling of any lattice parameters, which is commonly found in apatite-type structures. It is presumed that these reflections are associated with an unidentified lead oxychloride, and although only a small number of reflections of low intensity (as indicated in Fig. 3*b*) arise from this secondary phase they prevented detailed structural characterization of finnemanite. The refined lattice parameters and atomic positions for finnemanite and selected bond lengths and angles are in good agreement with those reported (Effenberger & Pertlik, 1979) for a natural specimen (Tables 5 and 6). As finnemanite crystals altered rapidly under electron irradiation, it was not possible to investigate the local structure.

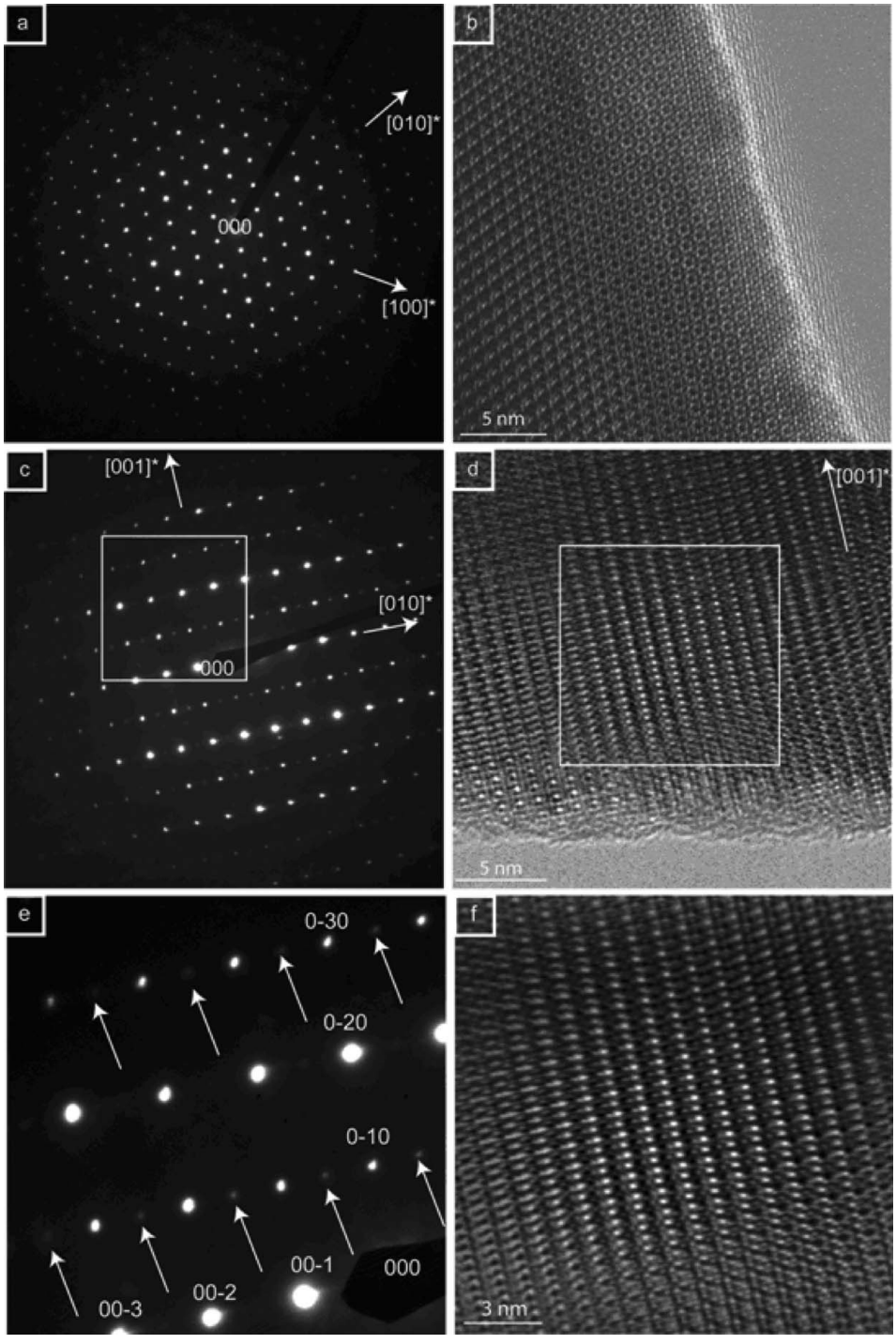

Figure 5
SAED and related HRTEM images of mimetite. (*a*) [001] mimetite SAED; evidence of dynamical effects are also present in the related HRTEM image (*b*). (*c*) [100] mimetite SAED where the dynamical effects aligned along [010]* and located at distances of *b*/2 are visible (enlarged inset *e*). The related HRTEM image (*d*) and its magnified inset (*f*) do not show contrast distribution related to the doubling of the *b* parameter observed in (*c*) and (*e*).

5. Valence and bonding

5.1. Chemical state of arsenic

Curve fitting of the XPS spectra for As 3(*d*) in $Pb_{10}(AsO_4)_6Cl_{1.48}O_{0.26}$ and $Pb_{10}(AsO_3)_6Cl_2$ revealed one binding-energy component, indicating that arsenic exists in a single chemical environment. Binding energies of As 3(*d*) were 45.2 eV for $Pb_{10}(AsO_4)_6Cl_2$ and 43.9 eV for $Pb_{10}(AsO_3)_6Cl_2$, corresponding to As^{5+} and As^{3+} species, respectively (Wagner *et al.*, 1979; Fig. 6). The Pb ($4f_{7/2}$) and Cl (2*p*) binding energies in finnemanite and mimetite invariably contained one component, consistent with the presence of Pb^{2+} and Cl^- (Fig. S2 of the supplementary material).

5.2. Bond-valence sums

Bond-valence calculations provide a simple way to monitor refinement quality and give insight into the nature of polyhedral distortions (Table 7). For the room-temperature mimetite the bond-valence sum for arsenic is close to pentavalence, while that for the tricapped metaprismatic Pb(1) columns indicate nominal underbonding. In these columns the Pb—Pb separations are 3.615 and 3.833 Å, thus defining the *c* repeat distance (~ 7.45 Å); however, these distances are too long for metal–metal interactions. After reduction to finnemanite, three O3 atoms at the end of the metprism prism are lost, resulting in dimerized truncated prisms. This process shortens the Pb—Pb distance to 3.43 Å which, as noted

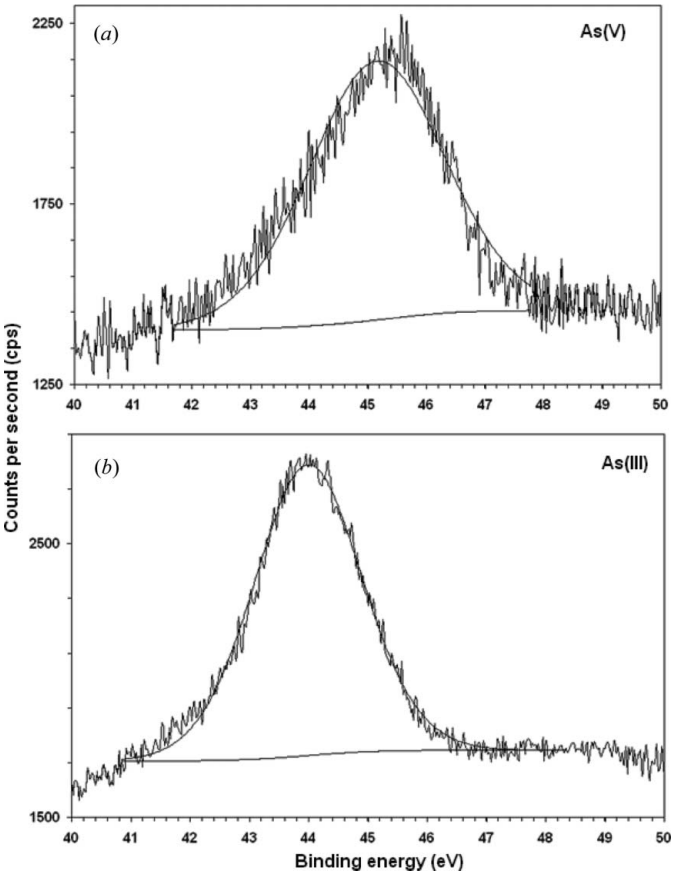

Figure 6
Arsenic 3(*d*) XPS spectra for (*a*) mimetite and (*b*) finnemanite.

by Effenberger & Pertlik (1979), is significantly shorter than that found in metallic lead. The bond-valence contribution for the Pb(1)—Pb(1) contact is 0.39 v.u. Pb(2) has an almost identical coordination in mimetite, however, there is an additional long contact to O3.

6. Conclusions

Near single-phase finnemanite $[Pb_{10}(As^{3+}O_3)_6Cl_2]$ has been synthesized as a reduced analogue of mimetite $[Pb_{10}(AsO_4)_6Cl_{1.48}O_{0.26}]$. A combination of powder neutron diffraction, electron diffraction and X-ray photoelectron spectroscopy found that both mimetite and finnemanite are hexagonal $P6_3/m$, however, splitting of the O3 atoms in mimetite gives rise to a possible doubling of the *b* axis, evident from SAED. The temperature-dependent transformation of clinomimetite to mimetite could not be verified. This more complete understanding of the crystallochemical relationship between mimetite and finnemanite should allow superior prediction of the long-term durability of hazardous waste forms.

This work was supported through a joint NRC-A*STAR research program on 'Advanced Ceramic Methods for the Co-stabilization and Recycling of Incinerator Fly Ash with Industrial Wastes'.

References

Baikie, T., Mercier, P. H. J., Elcombe, M. M., Kim, J. Y., Le Page, Y., Mitchell, L. D., White, T. J. & Whitfield, P. S. (2007). *Acta Cryst.* B**63**, 251–256.
Bauer, M. & Klee, W. E. (1993). *Z. Kristallogr.* **206**, 15–24.
Bruker AXS (2005). *TOPAS*, Version 3. Bruker AXS, Karlsruhe, Germany.
Calos, N. J. & Kennard, C. H. L. (1990). *Z. Kristallogr.* **191**, 125–129.
Cheary, R. W. & Coelho, A. (1992). *J. Appl. Cryst.* **25**, 109–121.
Dai, Y. S., Hughes, J. M. & Moore, P. B. (1991). *Can. Mineral.* **29**, 369–376.
Dong, Z. L., Sun, K., Wang, L. M., White, T. J. & Ewing, R. C. (2005). *J. Am. Ceram. Soc.* **88**, 184–190.
Dowty, E. (2002). *ATOMS*, Version 6.0. Shape Software, 521 Hidden Valley Rd, Kingsport, TN 37663, USA.
Effenberger, H. & Pertlik, F. (1979). *Tschermaks Miner. Petro. Mitt.* **26**, 95–107.
Elliott, J. C., Mackie, P. E. & Young, R. A. (1973). *Science*, **180**, 1055–1057.
Fairley, N. & Carrick, A. (2005). *The Casa Cookbook*, Part 1. Cheshire, England: Acolyte Science.
Ferraris, C., White, T. J., Plevert, J. & Wegner, R. (2005). *Phys. Chem. Miner.* **32**, 485–492.
Gonzales-Platas, J. & Rodriguez-Carvajal, J. (2006). *GFOURIER*, Version 04.05. Universidad de la Laguna, Tenerife, Spain.
Kampf, A. R., Steele, I. M. & Jenkins, R. A. (2006). *Am. Mineral.* **91**, 1909–1917.
Keppler, U. (1968). *Neues Jahrb. Miner. Monatsh.* pp. 359–362.
Keppler, U. (1969). *Neues Jahrb. Miner. Monatsh.* pp. 64–67.
Mackie, P. E., Elliot, J. C. & Young, R. A. (1972). *Acta Cryst.* B**28**, 1840–1848.
Pramana, S. S., Klooster, W. T. & White, T. J. (2007). *Acta Cryst.* B**63**, 597–602.
Pramana, S. S., Klooster, W. T. & White, T. J. (2008). *J. Mater. Chem.* In the press.
Sears, V. F. (1993). *International Tables for Crystallography*. Dordrecht: Kluwer Academic Publishers.
Stadelmann, P. (2003). *JEMS*, 12M-EPFL, CH-1015 Lausanne, Switzerland.
Suetsugu, Y. & Tanaka, J. (2002). *J. Mater. Sci. Med.* **13**, 767.
Wagner, C. D., Riggs, W. M., Davis, L. E., Moulder, J. F. & Muilenberg, G. E. (1978). *Handbook of X-ray Photoelectron Spectroscopy*. Perkin Elmer, Physical Electronics Division, Eden Prairie, MN.
White, T. J. & ZhiLi, D. (2003). *Acta Cryst.* B**59**, 1–16.
White, T. J., Ferraris, C., Kim, J. & Madhavi, S. (2005). *Rev. Mineral. Geochem.* **57**, 307.
White, T. J. & Toor, I. A. (1996). *J. Miner. Met. Mater. Soc.* **48**, 54–58.